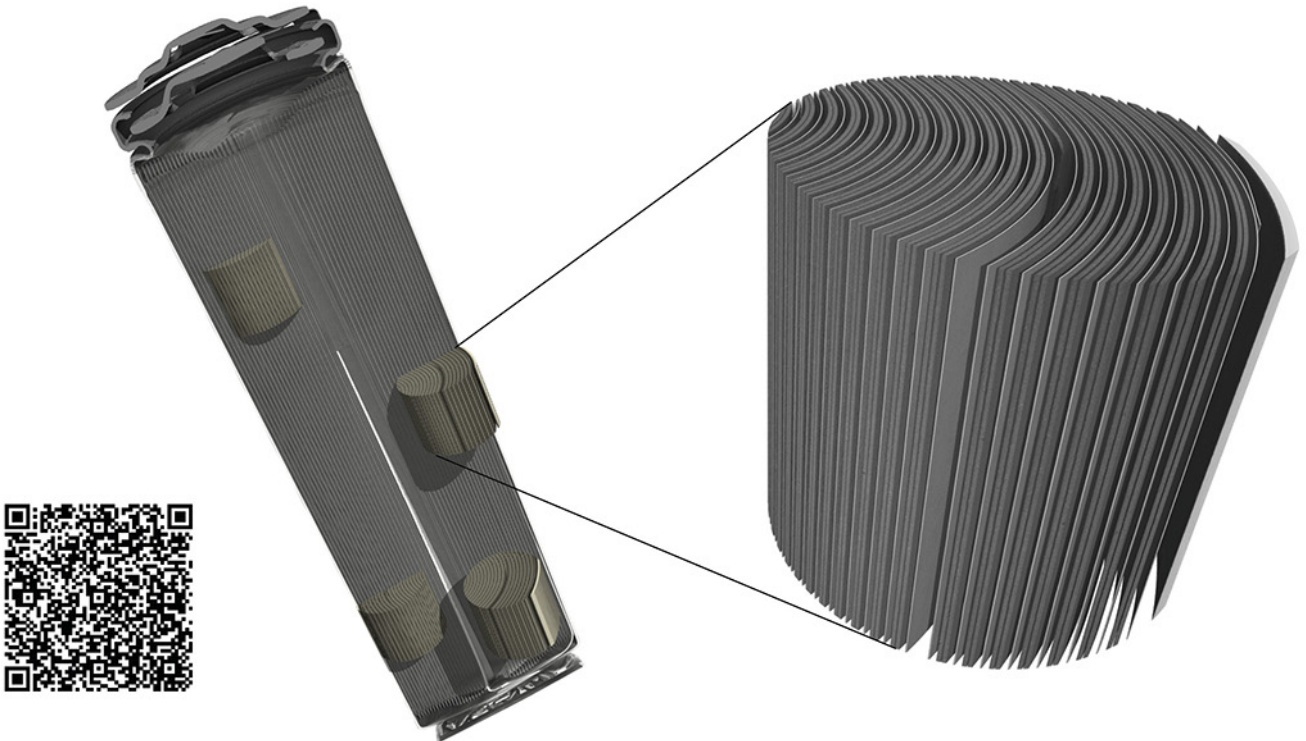


TESCAN micro-CT solutions

for energy storage materials research



TESCAN UniTOM XL

- ✓ Multi-scale non-destructive 3D imaging optimized to maximize throughput and contrast
- ✓ Fast scanning and high sample throughput with temporal resolutions below 10 seconds
- ✓ Wide array of samples types
- ✓ Enables dynamic tomography and *in-situ* experiments
- ✓ Dynamic screening for synchrotron beamtime
- ✓ Modular and open system with unmatched flexibility for research



[Click and find out more](#)

Investigating Degradation Modes in Zn-AgO Aqueous Batteries with In Situ X-Ray Micro Computed Tomography

Jonathan Scharf, Lu Yin, Christopher Redquest, Ruixiao Liu, Xueying L. Quinn, Jeff Ortega, Xia Wei, Joseph Wang, Jean-Marie Doux,* and Ying Shirley Meng*

To meet growing energy demands, degradation mechanisms of energy storage devices must be better understood. As a non-destructive tool, X-ray Computed Tomography (CT) has been increasingly used by the battery community to perform in situ experiments that can investigate dynamic phenomena. However, few have used X-ray CT to study representative battery systems over long cycle lifetimes (>100 cycles). Here, the in situ CT study of Zn–Ag batteries is reported and the effects of current collector parasitic gassing over long-term storage and cycling are demonstrated. Performance representative in situ CT cells are designed that can achieve >250 cycles at a high areal capacity of 12.5 mAh cm⁻². Combined with electrochemical experiments, the effects of current collector parasitic gassing are revealed with micro-scale CT. The volume expansion and evolution of ZnO and Zn depletion are quantified with cycling and elevated temperature testing. The experimental insights are utilized to develop larger form-factor (4 cm²) cells with electrochemically compatible current collectors. With this, over 500 cycles at a high capacity of 12.5 mAh cm⁻² for a 4 cm² form-factor are demonstrated. This work demonstrates that in situ X-ray CT used in long cycle-lifetime studies can be applied to examine a multitude of battery chemistries to improve performances.

1. Introduction

To address the growing energy concerns, high-performance and cost-effective energy storage solutions, such as batteries, need to be developed to enable technologies such as grid storage, Internet of Things, and high power electronics.^[1–3] While Li-Ion Batteries (LIBs) have received considerable attention due to their high energy densities, there are significant concerns surrounding the safety, recyclability, CO₂ footprint, and mining ethics of precious metals that warrant the development of alternative chemistries.^[4–9] With the benefits of lower material costs, benign chemistry, nonflammability, ambient processability, and high theoretical capacity (820 mAh g_{Zn}⁻¹, 5854 Ah L⁻¹), aqueous zinc batteries (aqZBs)^[10] are a promising alternative to LIBs.^[11–15] Additionally, given the higher ionic conductivities of aqueous electrolytes (≈1 mS cm⁻¹ for non-aqueous

LIB, ≈100 mS cm⁻¹ for aqZBs),^[12,13] aqZBs demonstrate superior performances in high current and pulse discharge applications in areas such as electric vehicles^[16] and high power electronics.^[17,18] Moreover, the benign chemistry and ambient processability allow for the development of flexible and stretchable batteries with easily adjustable form factors for applications in health monitoring and wearable electronics.^[17,19–21]

However, aqZBs suffer from poor cyclability and shelf-life, which originate from issues such as Zn anode shape change, dendrite growth, Zn dissolution, and parasitic gassing.^[20,22–25] To improve performances, several strategies have been explored to stabilize the anode and limit dendrite growth and anode shape change, such as the incorporation of additives in the electrode and electrolyte (e.g. Bi₂O₃,^[26,27] CTAB,^[28] Ca(OH)₂^[18,29,30] and polyethylene glycol (PEG)^[13,23,31]) and the development of novel 3D Zn sponge structures.^[16,32,33] Nevertheless, a deeper fundamental understanding of the anode degradation is needed to better improve performances.

The instability and corrosion of the Zn anode in basic electrolytes result in gassing and hydrogen evolution reactions (HER) (Equations 1,2),^[34,35]


J. Scharf, L. Yin, R. Liu, J. Wang, J.-M. Doux, Y. S. Meng
Department of Nano-Engineering
University of California San Diego
La Jolla, CA 92093, USA
E-mail: jdoux@eng.ucsd.edu; shmeng@ucsd.edu

C. Redquest
Department of Chemical Engineering
University of California San Diego
La Jolla, CA 92093, USA

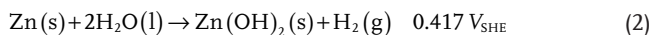
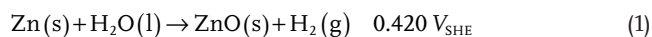
X. L. Quinn
Department of Materials Science and Engineering
University of California San Diego
La Jolla, CA 92093, USA

J. Ortega, X. Wei
Riot Energy Inc.
Camarillo, CA 93012, USA

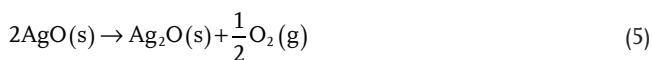
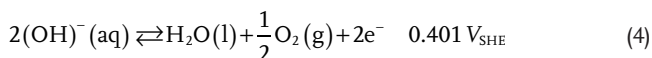
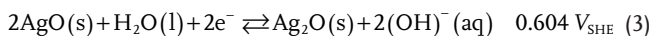
J. Wang, Y. S. Meng
Sustainable Power & Energy Center (SPEC)
University of California San Diego
La Jolla, CA 92093, USA

 The ORCID identification number(s) for the author(s) of this article can be found under <https://doi.org/10.1002/aenm.202101327>.

DOI: 10.1002/aenm.202101327



where V_{SHE} refers to the voltage versus a standard hydrogen electrode. As a result, electrolyte additives such as ZnO and LiOH are often employed to limit HER and anode corrosion.^[13] Cathode materials in aqZBs tend to suffer from oxygen evolution reactions (OER) caused by high cathode potentials.^[36] For instance, in Zn-Ag batteries, AgO offers a higher open-circuit voltage (OCP) than Ag₂O (1.86 V for AgO versus 1.56 V for Ag₂O) at nearly double the theoretical capacity (430 mAh g⁻¹ for AgO versus 230 mAh g⁻¹ for Ag₂O), and has demonstrated a high areal capacity of 54 mAh cm⁻² in a printable and flexible architecture.^[17,37–39] However, as shown in Equations (3,4), OER can facilitate AgO decomposition, resulting in capacity fade and self-discharge in Zn-AgO batteries.^[40,41]



OER can also increase the amount of dissolved oxygen in the electrolyte, facilitating the corrosion of the Zn anode.^[42] Furthermore, both OER and HER of non-active materials in

contact with the electrolyte, such as the current collectors, can limit the electrochemical performances of aqZBs.^[43] As Bonnick and Dahn showed, the parasitic gassing of the current collectors and casing in Ni-Zn coin cells can drastically influence the cycle life.^[44]

To investigate these degradation mechanisms, X-ray CT has been increasingly used in zinc-based battery research as a tool to probe and quantify valuable 3D morphological parameters, such as porosity and particle distribution.^[45–47] For example, CT has been used to show how the solid volume fraction in 3D porous Zn structures can improve the Zn Depth-of-Discharge (DoD_{Zn}) and energy density of anodes.^[45] Additionally, CT is ideal for in situ or operando studies due to its non-destructive nature, and since grey values in images are proportional to the material's X-ray attenuation, species can often be separated to observe the chemical evolution in electrodes. Franke-Lang et al., for example, were able to distinguish Zn from ZnO, and used in situ CT to visually investigate the degradation and volume expansion of a zinc-air battery.^[45] Likewise, Tobias et al. used *operando* CT to reveal Zn particle depletion to follow a core-shell model, in which ZnO continuously grows around and depletes the Zn particle core.^[46]

Most in situ X-ray CT studies of battery systems are limited to only the first few cycles,^[48,49] with few reports of long cycle life in situ CT studies (>100 cycles) that are representative of larger format cells and practical battery operation.^[50] Herein, we used in situ micro-scale X-ray CT (MicroCT) to study the effects of parasitic gassing on the performance of printed Zn-AgO batteries. As detailed in **Figure 1**, we developed in situ CT cells that are representative of previously reported cell performances^[17] to

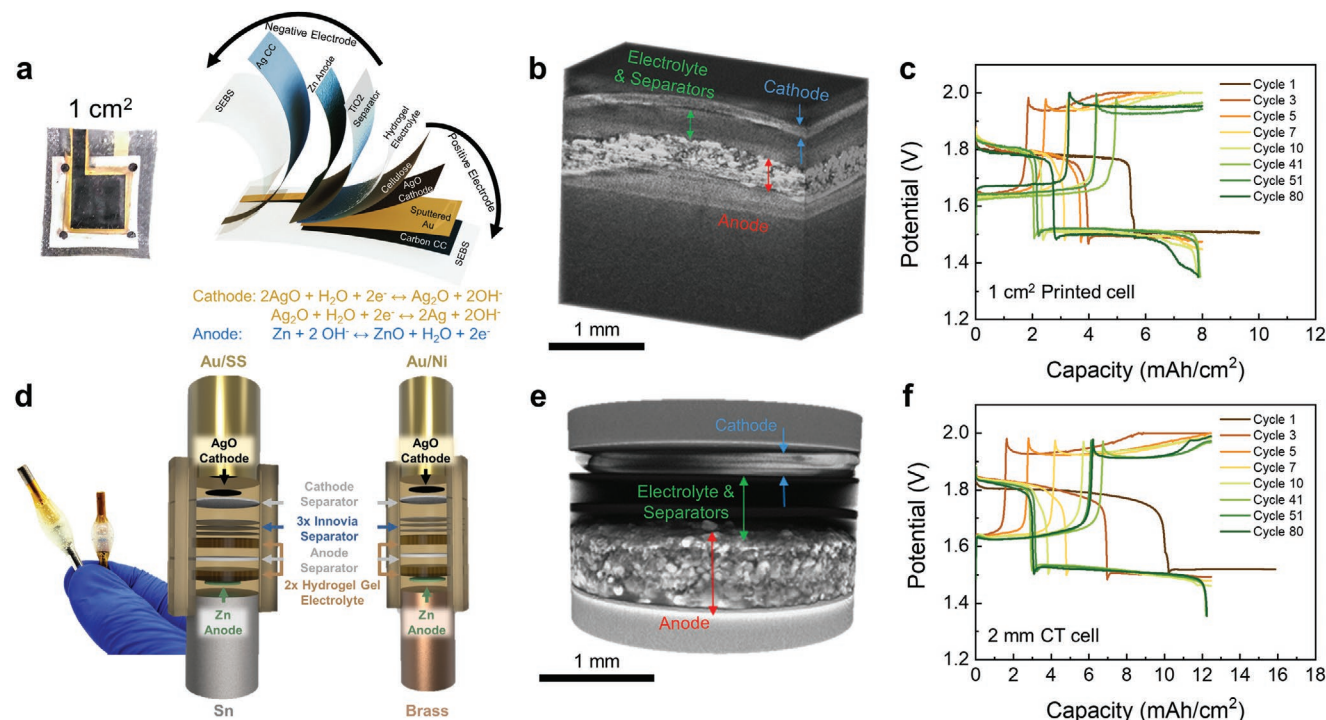


Figure 1. Comparison of the cell design and performances of the Zn-AgO printed cell (top—adapted with permission.^[17] Copyright 2020, Elsevier) and in situ CT cell (bottom). Comparison of a,d) cell architecture, b,e) 3D X-ray CT tomographic reconstructions, and c,f) electrochemical performances for Zn-AgO printed cell (top row) and in situ CT cell (bottom row).

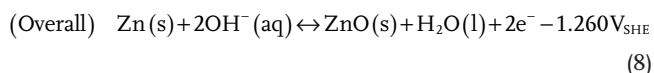
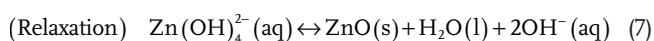
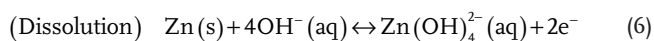
provide high-resolution scans and detailed analysis of the battery system. This CT cell design allows for longer cycling (>250 cycles) and was used to investigate the Zn particle development and growth of ZnO in situ with cycling. Finally, we showed how the insights of this study can be applied to larger-scale devices by demonstrating improved shelf and cycle life of a printed Zn-AgO battery.

2. Results and Discussion

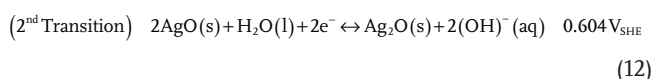
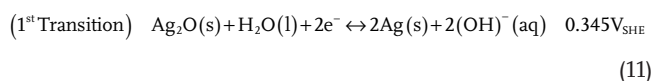
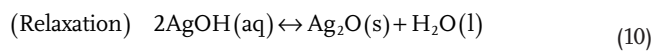
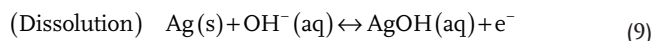
2.1. Current Collector Parasitic Gassing

In the Zn-AgO system, the redox reaction relies on the dissolution of zinc and silver species in the alkaline electrolyte and their supersaturation-induced precipitation, which takes place rapidly while maintaining a stable voltage (Equations (6–12)).^[39,40,51,52]

Anode



Cathode



As shown in Figure 1c,f, the first plateau corresponds to the first phase transition from AgO to Ag₂O (Equation 11), while the second corresponds to the transition from Ag₂O to Ag (Equation 12). To test the effects of OER and HER of current collector materials typically used in aqZBs,^[44] the current due to gassing was monitored through chronoamperometry (CA) and by applying potentials relevant to the reactions indicated above. The current density of the OER, after applying cathode-relevant potentials for 2 minutes on metal current collector rods, is presented in Figure 2a. Here, 0.2 and 0.5 V versus Hg/HgO corresponds to the first and second plateau of the cathode phase transition at 1.56 and 1.86 V versus Zn/ZnO respectively (Equations 11 and 12) and can be seen in Figure S7a, Supporting Information, at the minima points of the Tafel plot of the cathode. Likewise, Figure 2b shows the HER current density after a potential hold at the anode potentials indicated in the Tafel plot of the anode in Figure S7b, Supporting Information.

The same method was also used to test standard metal foils, and the results are shown along with the cyclic voltammetry (CV) in Figure S8, Supporting Information.

These results reveal higher OER gassing currents for bare materials than when electroplated with Au, which can also be seen in Figure S8g, Supporting Information, for metal foils that were sputtered with Au. However, the Au coated Ni (Au/Ni) yielded lower OER gassing currents than the Au coated Ti (Au/Ti) and Au coated stainless steel (Au/SS). On the anode end, brass and Sn rods were tested and compared. Brass rods were selected and used in the CT cells since they yielded lower HER gassing currents than copper when metal foils were tested (Figure S8h, Supporting Information). Brass rods showed lower HER currents than Sn but were similar in magnitude in the higher potential region (−1.45 V versus Hg/HgO).

To test the cycle reversibility of the anode with the different current collectors, Zn symmetric CT cells with Sn and brass rods were cycled at various DoD_{Zn} (Figure 2c,d). The anode films were initially discharged to half the desired DoD_{Zn} with a potentiostat in the basic electrolyte and then assembled in symmetric cells (Figure S4, Supporting Information). The first discharge was set to half the desired DoD_{Zn} to fully discharge one side to the set value and charge the other back to 0%. The cell was then cycled at the full desired DoD_{Zn}. As expected, a general trend was observed for both cases, in which higher DoD_{Zn} yielded less cyclability. The general failure mode for these cells appears to be capacity fade due to an over-oxidation of Zn and a build-up of a ZnO. However, cell shorting was observed for the brass-brass 40% DoD shown in Figure 2d and Figure S4e, Supporting Information. Yet, in both cases, the symmetric cells were able to cycle >100 cycles for a DoD of 10%, with the brass-brass symmetric cell achieving over 550 cycles. These results indicate good reversibility of the anode and suggest that the likely causes for failure in full cells originate at the cathode.

2.2. In Situ Micro-CT Analysis

The performance of full cells was evaluated using in situ MicroCT with two sets of current collectors, Sn with Au/SS rods (Sn-Au/SS) and brass with Au/Ni rods (Brass-Au/Ni), in order to determine the effects of current collector parasitic gassing. The architecture (Figure 1d) of the 2 mm diameter in situ cells was optimized to limit common issues, such as dendrite growth (Figure S1c,d, Supporting Information), so as to be representative of larger form factor performances. X-ray tomography was used to observe the evolution of the Zn anode during cycling. The various phases in the anode were separated using a reference containing Zn and ZnO powder (Figure S3, Supporting Information), and grey-value global thresholding was used to segment the Zn particles from the ZnO and the electrolyte-binder-pore (EBP) region as detailed in the methods section. A visualization of the segmentation process for the Sn-Au/SS case is detailed in Figure 3 and can also be seen in Video S1, Supporting Information.

As shown in Figure 4, CT full cells were scanned in situ at various points of cycling. The Sn-Au/SS CT full cell was only able to achieve ≈25 cycles, while the cell with less corrosive Brass-Au/Ni current collectors lasted ≈125 cycles before

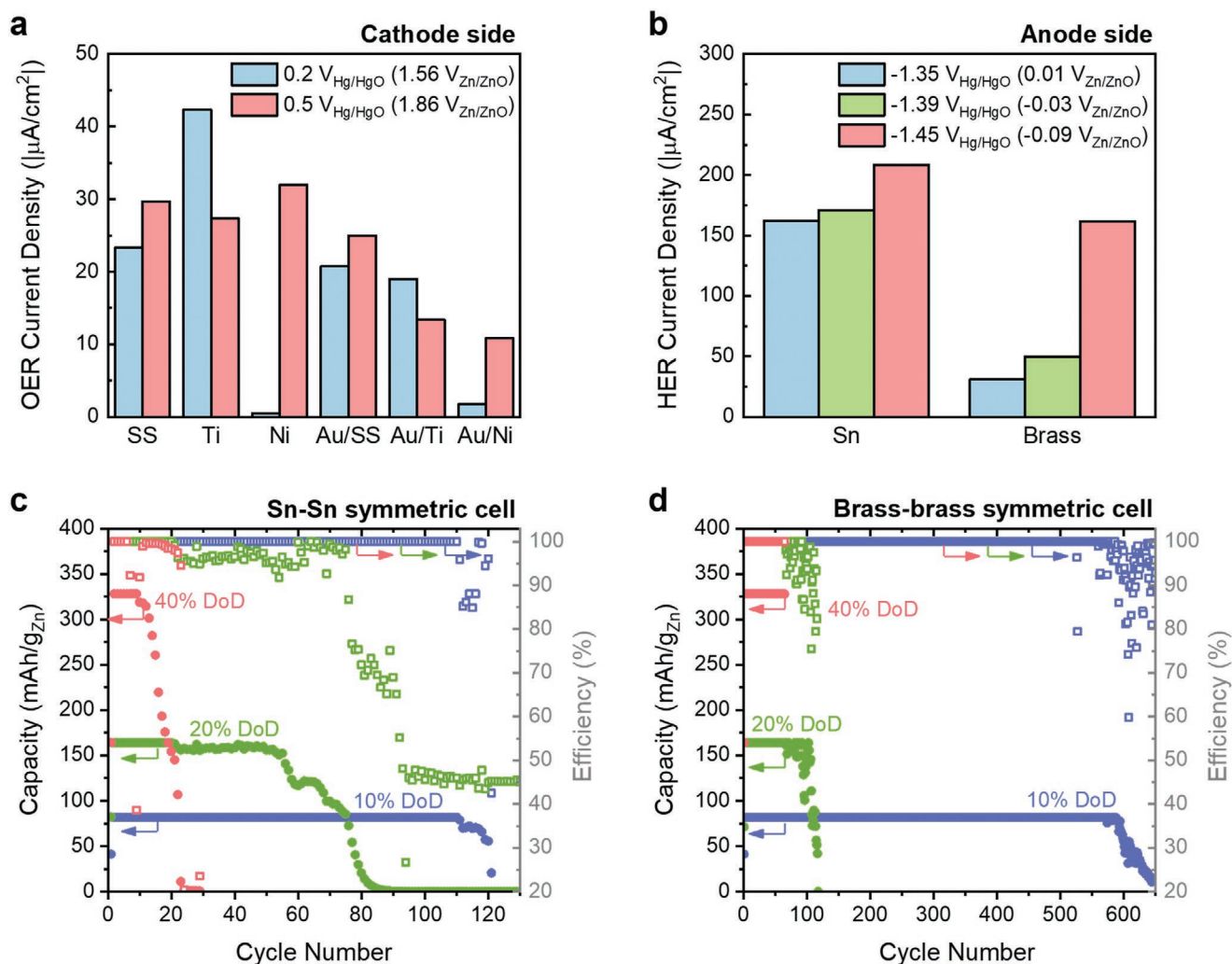


Figure 2. Current collector gas evolution. Gassing currents after 2 min of CA for a) OER at cathode relevant potentials and b) HER at anode relevant potentials. Anode symmetric cell cycling performances with c) Sn current collectors and d) brass current collectors.

starting to exhibit capacity fade. The various species (Zn, ZnO, and EBP) were colorized in the XZ cross-sectional slices and 3D tomograms of Figure 4c,d. The quantitative analysis is presented in Figure 5a: it reveals an increase of ZnO with cycling for both cells, confirmed by the increasing impedance of both cells during cycling (Figure S1f, Supporting Information) resulting from the buildup of the insulating ZnO. The XZ slices show a clear increase of ZnO formation (along with a decrease of Zn) near the current collectors, whereas Zn particles near the electrolyte interface are retained at longer cycle lifetimes. This disproportionate depletion of Zn and growth of ZnO near the metal interface could suggest the effects of current collector gassing or electron transport limitations in the depletion of the active material at the anode.

When comparing the two current collector cases, more Zn and less ZnO are observed for the Brass–Au/Ni cell at the same cycles (e.g., at cycles 11 and 30). Furthermore, the EBP volume fraction stays constant after the 11th cycle, showing the increase of ZnO as the main culprit for the volume expansion and the thickness increase shown in Figure 5b. Our results show the

Zn anode volume expansion to be around 100%, which is similar to the 60–70% reported by Tobias et al. for an aqueous alkaline Zn–Air system.^[46]

The size of the Zn particles, as depicted in Figure 4e, decreases with cycling. For the Sn–Au/SS, there was still a considerable amount of Zn still left after cell failure at 30 cycles. However, for the Brass–Au/Ni cell, more of the Zn was utilized, and by cycle 101, nearly all of it is converted to ZnO. This is shown in Figure 5c, where the equivalent diameter of the Zn particles shrinks as a function of cycling, and the Brass–Au/Ni cell can cycle longer to utilize more of the Zn particles. Fits for the particle size distribution for the two current collector cases can be seen in Figure S10, Supporting Information. For the Brass–Au/Ni cell, the particles are still densely packed at cycle 11, with little ZnO, as they were when first fabricated (Figure S2a,d, Supporting Information). The particle-scale tomograms (Figure 4f) reveal that as the cell continues to cycle, more ZnO grows around the Zn particles as the core is depleted, thus following a core-shell model as observed by Tobias et al.^[46]

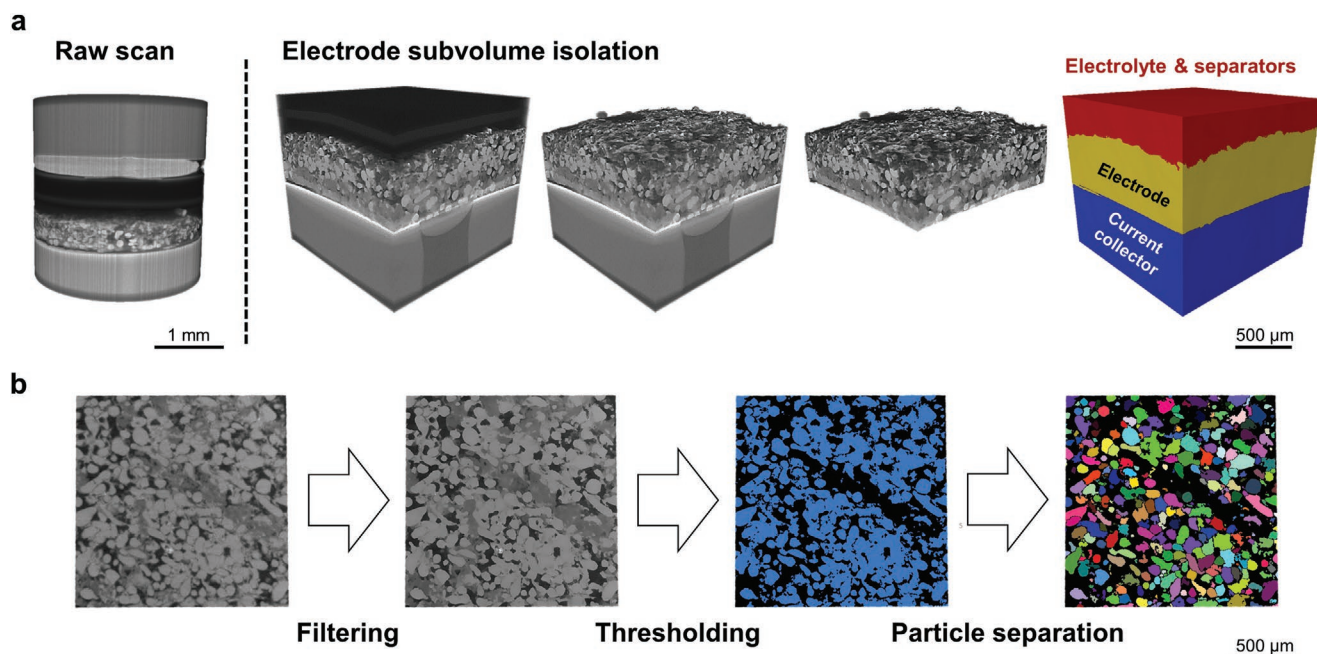


Figure 3. MicroCT segmentation and analysis procedure. a) Cropping and segmentation workflow to analyze anode region of a battery after the 11th discharge, using the Sn–Au/SS current collectors. On the right, the electrolyte and separator region is represented in red, the anode in yellow, and the Sn current collector in blue. b) Filtering, thresholding, and Zn particle separation workflow used to analyze the Zn particle size distribution of the anode. The process is here demonstrated on the electrode after the 11th discharge.

2.3. Effects of Current Collector on Shelf and Cycle Life

The symmetric cycling of Figure 2 suggests that the cell performance is limited by effects on the cathode side. As such, the effects of the cathode current collector on the shelf life and cycling performances were investigated for cells with Au/Ni and Au/SS current collectors. The anode current collectors were fixed to Cu, which was chosen over brass to avoid any side reaction with the electrolyte as brass contains Zn. The shelf life performances of the cells were evaluated by monitoring OCP with time at elevated temperatures. CT cells constructed with Au/Ni and Au/SS current collector rods were monitored for two weeks at 40 °C. As shown in Figure 6a, the Au/Ni cell exhibited less self-discharge before transitioning to the second plateau. After two weeks, CT scans were taken of the two cells, and the 3D reconstructed tomograms of the anodes were compared. The colorized XZ slices, 3D tomograms, and volume fraction percentage in Figure 6b,c reveal more ZnO (and less Zn) for the cell with the Au/SS current collector. Additionally, compared to the pristine case, the Au/SS cell exhibited larger Z-axis volume expansion than the Au/Ni cell. The increase of ZnO can be explained by Zn anode corrosion, originating from an increase of dissolved oxygen from the OER reaction of the cathode current collector.^[42]

Ultimately, the results from the X-ray CT experimentation reveal parasitic current collector gassing to be a key degradation mechanism for both cycle and shelf life. As a result, larger 4 cm² form-factor cells were constructed and the effects of current collector parasitic gassing on electrochemical performance were examined. This was done to ensure the insights gained from CT and the smaller 2 mm in situ cells extend to larger

practical-scale battery systems. To test the self-discharge, shown in Figure 6d, these larger form-factor cells were left to age at various temperatures while the OCP was monitored. At each temperature, the Au/SS cells fail quicker than the Au/Ni cells. The rapid drop in voltage shown for the Au/SS cell at 55 °C is likely caused by electrolyte depletion due to increased gassing at higher temperatures and is thus indicative of cell degradation or failure. However, due to less gassing, the Au/Ni cell at 55 °C demonstrated self-discharge with the expected two-phase transition. The Direct Current Internal Resistance (DCIR) was also monitored during the OCP measurement in Figure S6a, Supporting Information. The Au/SS cells quickly exhibited large increases in resistance whereas the Au/Ni cells increased slowly or were stable with time. The self-discharge rate for the Au/Ni cell at room temperature was quantified by discharging cells after controlled idle times to measure the percent of capacity loss with time. A discharge was performed every week over 4 weeks, and the results in Figure S6c,d, Supporting Information, reveal an average discharge rate of 7.06% wk⁻¹, a considerable improvement with respect to previously reported lifetimes.^[41,53]

The cycling performance of the cells with improved current collectors (Cu–Au/Ni) was also evaluated. Figure 7 compares the cycling of larger form factor cells with the smaller scale in situ cells fabricated for CT. The 1 cm² cell, cycling at ≈8 mAh cm⁻² in grey, are the results of a Zn–AgO battery developed during our previous work with non-optimized current collectors.^[17] Compared to this cell that demonstrated 80 cycles, both the CT and the 4 cm² cell with more electrochemically compatible current collectors demonstrated more than 250 cycles with capacity retention exceeding 80%. The slight dip in coulombic efficiency observed, for example at around 50 cycles for the CT

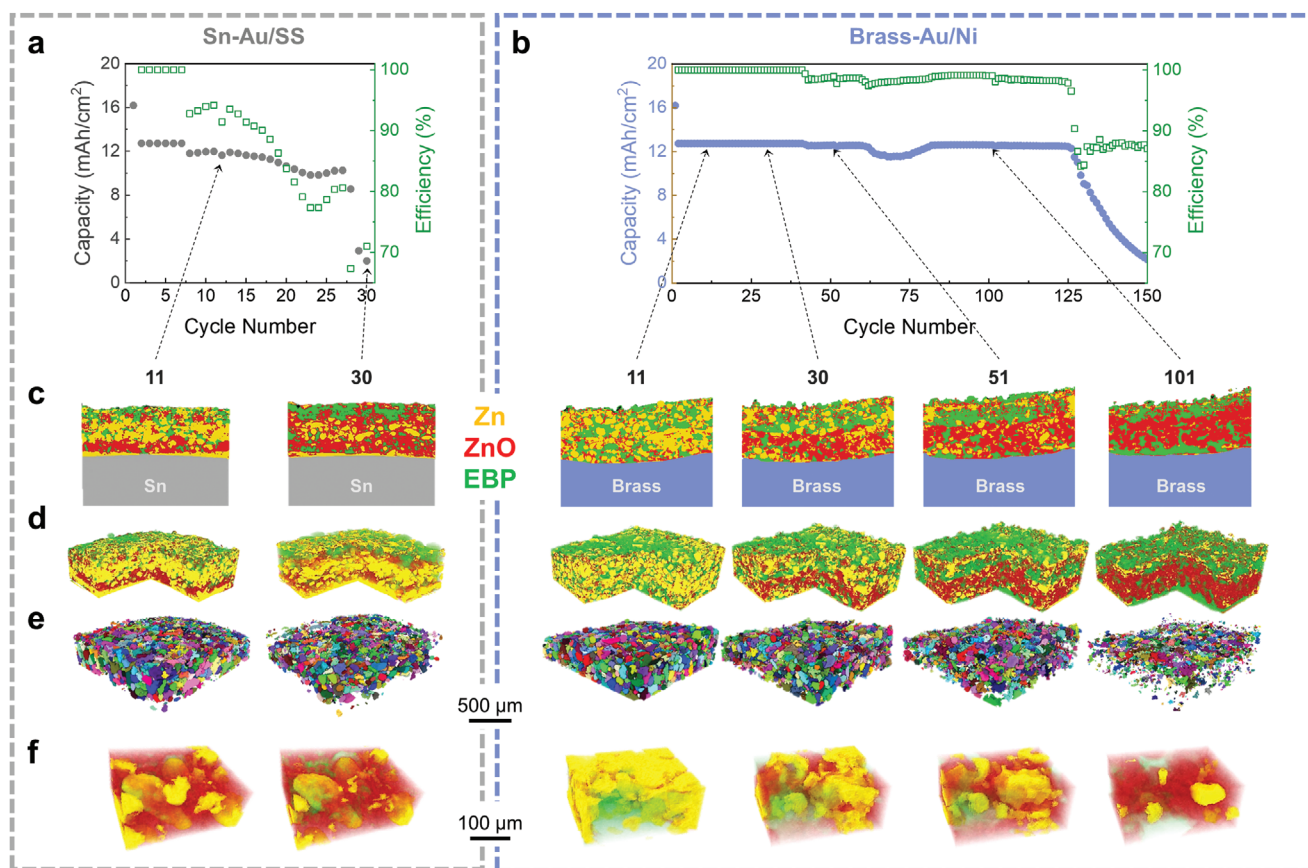


Figure 4. In situ MicroCT analysis. Electrochemical cycling performance of in situ MicroCT cells with a) Sn and Au coated stainless-steel current collectors and b) Brass and Au coated Ni current collectors. MicroCT analysis at specified cycles: c) colored XZ slices of Zn anode, d) colored corner-cut 3D reconstructed volumes of Zn anode, e) segmented Zn particles, and f) colored particle scale 3D renderings. Segmentation of Zn (yellow), ZnO (red), and EBP (green) in XZ slices and volume rendering is based on global thresholding. Zn particles in e) are indistinctly colored to showcase separation of individual particles.

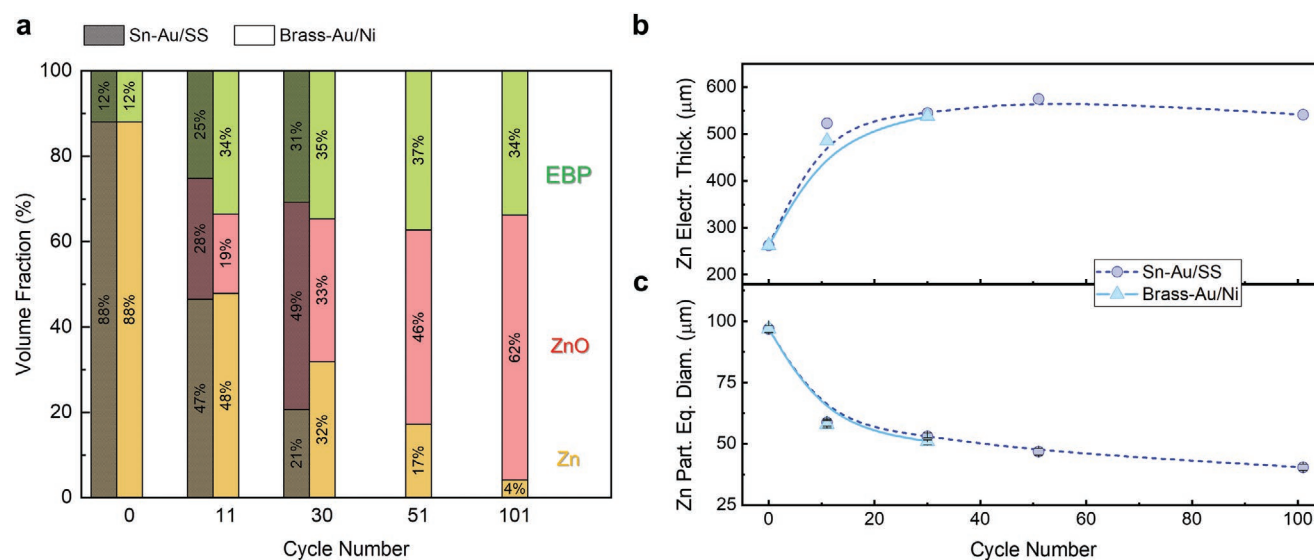


Figure 5. Extracted X-ray CT Statistics. a) Anode volume fraction of Zn (yellow), ZnO (red), and EBP (green), b) Zn anode electrode thickness, and c) Zn particle equivalent diameter evolution during cycling. In situ CT cells with Sn and Au-coated stainless-steel current collectors are represented by solid lines and triangle markers while cells Brass and Au-coated Ni current collectors are represented by dashed lines and circle markers.

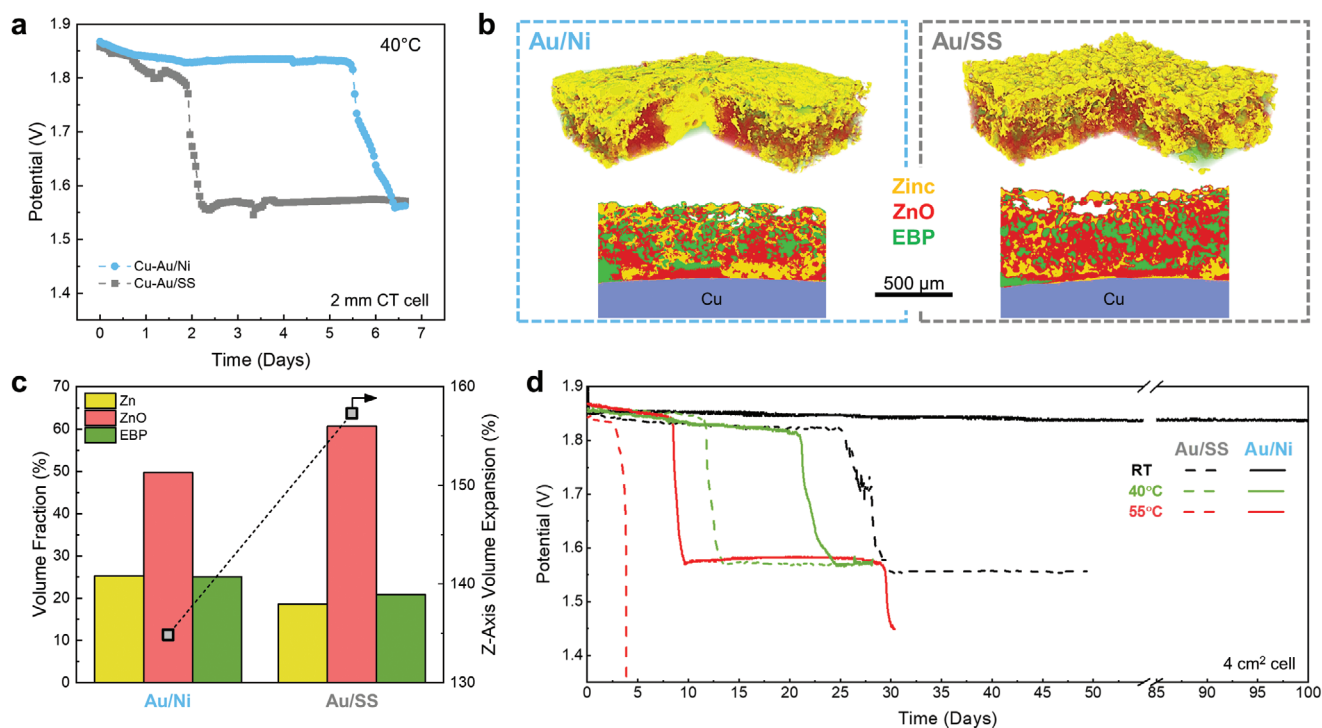


Figure 6. Shelf life and effect of current collector. a) Open-circuit voltage at 40 °C of 2 mm diameter in situ CT cell with Au coated Ni (blue) and Au coated stainless-steel (grey) cathode current collectors. b) XZ CT slice and colored corner-cut reconstructed volume and c) volume fraction (left) of Zn (yellow), ZnO (red), and EBP (green) and z-axis volume expansion (right) of Zn anode after 1 week at 40 °C. d) Open-circuit voltage of larger 4 cm² cells at room temperature, 40 and 55 °C for different cathode current collectors.

cell, is due to the transition between the capacity-limited regime and the voltage limited regime.^[17] With the optimized current collector, the 4 cm² form factor in Figure 7b illustrates superior performances, >275 cycles at C/5 (2.5 mA cm⁻²), >500 cycles at C/3 (4.17 mA cm⁻²), >300 cycles at C/2 (6.25 mA cm⁻²). The low impedance of this cell (Figure S6b, Supporting Information) with optimized current collectors allows for higher rate cycling, which is also revealed in the capacity-voltage plot in Figure S11f, Supporting Information, by the small IR drop when cycling at 6.25 mA cm⁻². Overall, the cell demonstrated a cycling volumetric energy density of 98.6 Wh L⁻¹ and power density of 49.3 W cm⁻³ (Table S1, Supporting Information).

3. Conclusion

In this work, we used in situ X-ray MicroCT in combination with electrochemical experiments to investigate the effects of current collector gassing on the performances of Zn–AgO batteries. The results reveal the importance of choosing electrochemically compatible current collector materials in limiting OER and HER reactions that degrade cell performances. With in situ MicroCT, we quantified the Z-axis volume expansion and showed Zn particle depletion with cycling that follows a shrinking core model. From an improved selection of electrochemically compatible current collectors, we demonstrated superior performances with a high cycling capacity of 12.5 mAh cm⁻² for more than 500 cycles in a 4 cm² form factor. This resulted in a cycling volumetric energy density of

98.6 Wh L⁻¹ and power density of 50.3 W cm⁻³. We have demonstrated extended cycle and shelf life enabled by the mitigation of the current collector gassing and have successfully prolonged the lifetimes of Zn/AgO batteries.

However, while we demonstrated a self-discharge rate of 7.06% wk⁻¹, further efforts are required to extend cell shelf life further. The investigation on the Zn symmetric cells and shelf-life tests showed that the OERs at the cathode current collector are one of the limiting factors. As a result, current collector treatments and coatings need to be developed to limit the OER and improve performances. Additives in the electrodes and the electrolyte also need to be explored to limit parasitic reactions, and further investigations of electrochemically compatible hydrogels could limit silver dissolution known to degrade Zn–Ag battery performances.

Lastly, through the development of representative in situ CT cells, we report the first in situ CT study of Zn–Ag batteries and utilize CT to study the degradation with long-term cycling (>250 cycles at 12.5 mAh cm⁻²). The results from this work exemplify the utility and advantages of in situ CT experimentation in elucidating degradation effects in battery systems. Following this work, we expect lab-scale in situ CT to be increasingly used in academic and industry battery research to better improve device performances and aid in the effort to combat the energy crisis.

4. Experimental Section

Fabrication and Synthesis of Cell Components: The electrodes were fabricated in similar ways compared with those in the previous work.^[17]

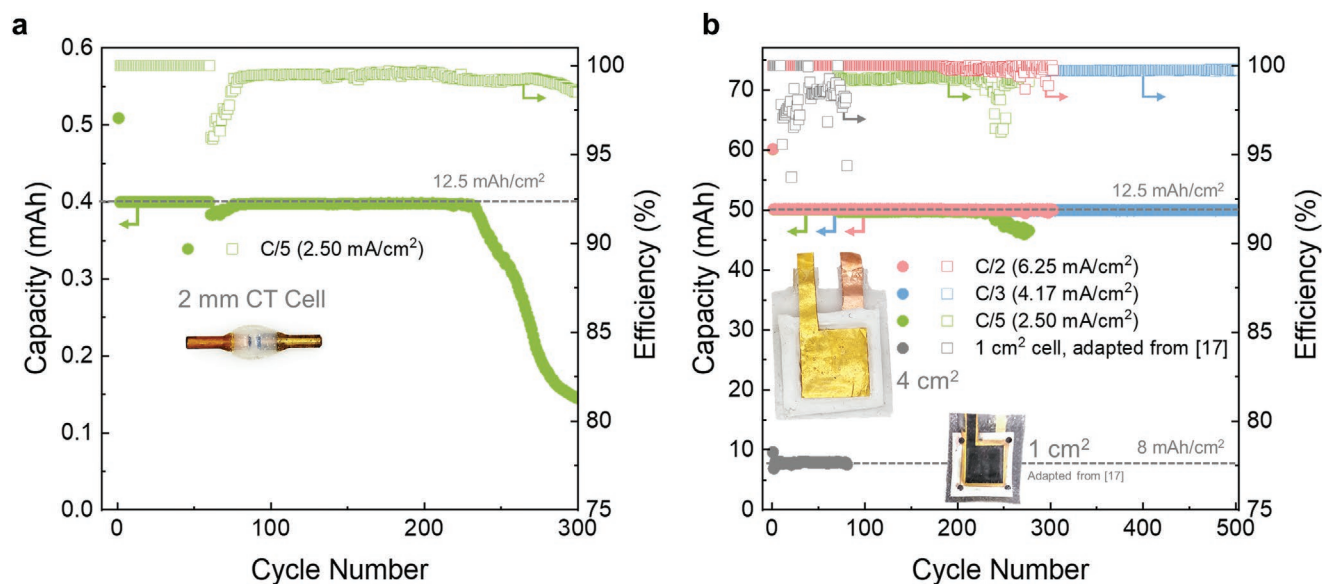


Figure 7. Cycle life performance. Electrochemical cycle life of a) 2 mm diameter in situ Au/Ni-Brass CT cell and b) larger 4 cm² Au/Ni-Cu cell and 1 cm² cell adapted with permission.^[17] Copyright 2020, Elsevier, with unoptimized current collectors.

A binder resin was prepared by dissolving 1 g GBR-6005 fluorine rubber in 2.75 g acetone. The cathode slurry was prepared by mixing 0.95 g AgO powder and 0.05 g Super-P powder, followed by adding 1.25 g binder resin and mixing in a planetary mixer (Flaktak Speedmixer™ DAC 150.1 FV) at 2500 rotations per minute (rpm) for 10 min. The anode slurry was prepared by mixing 0.91 g Zn powder and 0.09 g Bi₂O₃ powder, followed by adding 0.25 g binder resin and mixing in a planetary mixer at 1800 rpm for 5 min. Both slurries were then cast using a doctor blade, cured at 80 °C for 30 min, and trimmed into the desired shape for later use.

The synthesis of the PVA hydrogel, serving as a barrier to prevent dendrite growth, is adapted from the previous work.^[17] A PVA solution was prepared by dissolving 1 g of PVA in 5 g of deionized water, and a hydroxide solution was prepared by dissolving 0.2 g Ca(OH)₂, 0.109 g LiOH, and 5 g KOH in 26.159 g deionized water and removing any precipitated solid. The LiOH and Ca(OH)₂ were introduced in the electrolyte in order to remove dissolved CO₂ and reduce anode shape change, respectively. The hydroxide solution was then added to the PVA solution in a 15.775:10 weight ratio while stirring to obtain the hydrogel precursor. The precursor was then placed in a Patri dish in a vacuum desiccator to dry and crosslink until only 27.62% of the original weight was left. The gel was then cut to the desired size and stored in a 10 M KOH + 0.6 M LiOH solution at 20 °C.

CT Cell Construction: The in situ cells were constructed using PTFE tubing with a 4 and 3 mm inner diameter for the Sn–Au/SS and Brass–Au/Ni respectively. The following metallic current collector rods were purchased from McMaster-Carr: 18-8 stainless steel, grade 2 titanium, 400 nickel, 360 brass, and 110 copper. The Sn rods were fabricated in-house by melting lead-free solder (99% Sn, .3% Ag, .7% Cu) and using the PTFE tubes as molds for making 4 and 3 mm inner diameter rods. Gold electroplating was performed on the cathode rods using commercial plating solutions.^[54] Before plating, the rods were first electro-cleaned at –2 V versus stainless steel for 2 min. The stainless-steel rods then underwent an extra nickel strike step for 2 min at –2 V versus stainless steel to facilitate the adhesion of the Au. Lastly, the rods were electroplated using a potassium aurocyanide solution by applying –1.5 V versus a platinum counter electrode for 20 min. The calculated thickness from the coulomb count and the surface area of the rods was determined to be ≈500 nm. A picture of all the current collector rods is presented in Figure S1a, Supporting Information.

The active material was punched smaller than the current collectors, with a 2 mm diameter, and placed directly onto the rods. For a direct

comparison of the device performance, both devices in the in situ study of Figure 4 used the same batches of anode and cathode material. Similarly, the active materials used in the CT cells of Figure 5 were of the same batch. Commercial separators were supplied by Riot Energy Inc.: 1) Flexible Alkaline Separator film that was used as the anode separator, consisting of a microporous polyolefin film with an inorganic filler,^[55] 2) a cellophane-based film (Innovia Films Company) that was used to help block silver migration,^[56,57] and 3) a microporous EVOH film to separate the cellophane separator from the cathode. The order of layers for the in situ cells is outlined in Figure 1d. The hydrogel electrolyte and separators were punched to the size of the tube diameter, larger than the active material to prevent crossover of Zn and Ag species around the edges. A 60% weight ratio of gel electrolyte to active material was found to properly wet electrodes for adequate cycling. The anode-cathode ratio was kept at approximately 5:1 to cycle the anode at ≈10% DoD_{Zn}. For consistency, the same weight percentages and ratios of the active material and electrolyte were used for the 4 cm² form factor cells. After assembly, commercial epoxy (Gorilla Glue) was used to seal the cells from end to end to avoid electrolyte leakage.

4 cm² Form-Factor Cell Construction: The larger form factor cells were constructed with 4 cm² metal foil current collectors with a 0.4 cm × 3 cm tab to allow for electrical contact (See Figure S5a, Supporting Information). The foils were placed on a Styrene-ethylene-butylene-styrene (SEBS) thermo-elastomer substrate with epoxy (Gorilla glue) applied to the tab regions to allow for better sealing of the metals. Following this, the active materials were added atop the foils with 25 μL of liquid electrolyte (10 M KOH, 0.6 M LiOH) applied to the cathode to enhance wetting. Next, the PVA hydrogel electrolyte and separators were added. The anode and cathode stacks were then joined, and the SEBS sheets were vacuum- and heat-sealed (Figure S5b, Supporting Information). A final layer of wear-resistant nylon (McMaster-Carr) was then added and vacuum and heat-sealed outside the SEBS sheets to ensure robust sealing. The final cell measured 3.5 × 3.5 cm² with a thickness of 2.05 mm, and an active area of 2 × 2 cm².

The following metal foils were used, without any coating unless specified otherwise, in the assembly of the 4 cm² cells and in electrochemical testing: 18-8 stainless steel (McMaster-Carr), 99.99% titanium (Amazon), nickel 200/201 (McMaster-Carr), 260 brass (McMaster-Carr), 99.99% Copper (MTI), and 99.99% Tin (Amazon) with thicknesses of 25–30 μm. For the gold-coated foils (Ni, Ti, or stainless steel), ≈500 nm of Au was sputtered with a thin Ti adhesion layer at an Ar gas flow rate of 16 SCCM. A DC power of 200 and 300 W was used for

the Au and Ti sputtering respectively. The sputtering was performed with a Denton Discovery 635 Sputter System (Denton Discovery 635 Sputter System, Denton Vacuum, LLC, Moorestown, NJ, USA).

Cell Cycling Protocol: All cells followed the same cycling protocol and were cycled using Neware BTS4000-5V10mA (dual range) and BTS4000-5V50mA (dual range) systems. In the first cycle, cells were initially discharged with a constant current to 60% of the cathode theoretical capacity. Following this, cells were cycled at 50% of the cathode capacity with a voltage cutoff of 1.35 V when discharging, and a 2 V constant voltage limit during charging to limit OER and water splitting. The in situ cells were initially discharged during the first cycle at C/10 (1.25 mA cm⁻²) and then cycled at C/5 (2.5 mA cm⁻²) for the remainder of the cell life. The 4 cm² form factor cells were initially discharged at C/10 and then cycled at C/5 for 10 cycles before cycling at the specified rate (i.e., C/3 or 4.17 mA cm⁻²). The self-discharge rate was determined by letting the 4 cm² cells rest for 1, 2, 3, and 4 weeks at room temperature (Figure S6c,d Supporting Information) before they were discharged at 2 mA (0.5 mA cm⁻² or C/50) to a voltage cutoff of 1 V.

The open-circuit potential (OCP) measurements presented in Figure 6a,d were performed using a Landt battery test system (Landt Instruments CT2001A). The cell open-circuit voltage was measured every 1 h. The DCIR used to probe the DC resistance in Figure S6a, Supporting Information, was performed using a 5 mA/10 mA pulse. The elevated temperature OCP was performed using a temperature chamber with precise control from 0 to 65 °C. Galvanostatic-EIS (GEIS) measurements were performed on both the in situ and 4 cm² cells using a Biologic-SPI50 Potentiostat. Scans were performed from 1 MHz to 1 Hz with 10 points per decade, an average of 8 measures per frequency, and an AC amplitude of 30 μA and 200 μA for in situ CT cells and 4 cm² cells respectively.

CV and CA measurements were performed in an aqueous electrolyte (10 M KOH, 0.6 M LiOH) in a three-electrode configuration with a Hg/HgO reference electrode and a platinum foil counter electrode. The electrochemical stability of the foils was tested first with a 1 min OCP to ensure stability of the reference electrode and was followed by 5 cycles of CV (Figure S8, Supporting Information). The anode was scanned from -1.0 to -1.5 V versus Hg/HgO at a rate of 100 mV s⁻¹ and the cathode from 0.0 to 0.7 V versus Hg/HgO at a rate of 10 mV s⁻¹. Following this, CA was applied for 2 min at the following potentials with a 1 min OCP performed in between: 1) -1.35 V, -1.39 V, and -1.45 V versus Hg/HgO for the anode current collectors, 2) 0.2 V, 0.5 V, and 0.6 V versus Hg/HgO for the cathode current collectors.

X-Ray CT Experimentation and Analysis: The scans were performed with a ZEISS Xradia 510 Versa MicroCT instrument, and parameters were kept consistent between each scan at the various SOCs. An X-ray energy of 140 kV was used at 10 W (71.56 μA) with a voxel size of 2.504 μm, a FOV of 2.48 mm × 2.52 mm, a 1.5 h scan time, a 4× magnification, an exposure time of 2 s, a binning of 2, and 1600 projections. The source to detector distance was also kept the same at 30.80 mm to ensure similar grey values between scans. No beam hardening correction was necessary during reconstruction. The two in situ CT cells in Figure 4 were scanned at the end of the discharge at different points of cycling: 1) after cycles 11 and 30 for the Sn-Au/SS cell, and 2) after cycles 11, 30, 51, and 101 for the Brass-Au/Ni cell. The initial or pristine case was performed on the bare anode from the same batch used in the respective cells (Figure S2a, Supporting Information).

MicroCT data analysis was performed with Amira 2019 commercial software. Tomograms from the same device, but scanned at different cycles, were aligned using the “Register Images” module which uses an iterative optimization algorithm to align datasets.^[58–61] After alignment, the datasets were cropped with a 600 × 600 pixel window (1.5 mm × 1.5 mm) in the XY direction to remove edge effects (Figure 3). With thresholding and area selection interpolation, the anode was analyzed separately by disregarding the electrolyte and current collector regions above and below the anode in the Z direction. The volume of each anode was then analyzed, and the average thickness was determined by dividing the total anode volume by the XY window.

Once isolated, the following Amira filters were applied to the reference and every anode was analyzed to ensure grey-scale values were

comparable: 1) Non-Local Means, 2) Unsharp Mask, 3) Delineate. As shown in Figure S3b, Supporting Information, once filtered, 3 distinct peaks pertaining to the Zn, ZnO, and EBP regions were visible. Global thresholding was then used to separate the three regions, and the “Volume Fraction” module was implemented to quantify the percentage of each species within the anode. The “Separate Objects” module, which implements a combination of watershed, distance transforms, and numerical reconstruction algorithms, was used on the Zn region to separate the particles. It is important to note that in this work CT was utilized to investigate meso-scale and bulk morphological changes of the Zn and ZnO species, and nano-structured Zn morphologies observed in Zn-based batteries,^[18,62,63] smaller than the ≈5 μm resolution of the CT scans, were not considered.

Trainable Weka Segmentation, an open-source convolution method which uses machine learning, was also explored and compared with global thresholding as method for species segmentation of the Zn anode. Shown in Figure S9, Supporting Information, Trainable Weka Segmentation of the anode was compared with threshold segmentation for the Sn-Au/SS in situ cell after the 11th discharge. The species volume fraction and Zn particle equivalent diameter (Figure S9a,b, Supporting Information) were remarkably similar. Additionally, there was no significant difference in the segmented tomograms or XY slices shown in Figure S9c, Supporting Information.

Supporting Information

Supporting Information is available from the Wiley Online Library or from the author.

Acknowledgements

This work was supported by funding from Riot Energy Inc., USA and Qualcomm, USA. For use of the MicroCT system, the authors would like to acknowledge the National Center for Microscopy and Imaging Research (NCMIR) technologies and instrumentation are supported by grant R24GM137200 from the National Institute of General Medical Sciences. This work was performed in part at the San Diego Nanotechnology Infrastructure (SDNI) of UCSD, NANO3, a member of the National Nanotechnology Coordinated Infrastructure, which is supported by the National Science Foundation (Grant ECCS-1542148). The authors would also like to acknowledge Neware Technology Limited for the donation of CT4000 battery cyclers, which are used to obtain the cycling data of cells in this paper.

Conflict of Interest

The authors declare no conflict of interest.

Data Availability Statement

Research data are not shared.

Keywords

corrosion, in situ characterization, x-ray computed tomography, zinc, Zn-based batteries

Received: April 27, 2021

Revised: June 9, 2021

Published online:

- [1] P. Jiang, Y. V. Fan, J. J. Klemesš, *Appl. Energy* **2021**, *285*, 116441.
- [2] T. Ahmad, D. Zhang, *Energy Reports* **2020**, *6*, 1973.
- [3] A. Foley, A. G. Olabi, *Renewable Sustainable Energy Rev.* **2017**, *68*, 1112.
- [4] L. Talens Peiró, G. Villalba Méndez, R. U. Ayres, *JOM* **2013**, *65*, 986.
- [5] A. Eftekhari, *ACS Sustainable Chem. Eng.* **2019**, *7*, 5602.
- [6] Calls for lithium battery review after Boeing Dreamliner fire at Heathrow | Boeing | The Guardian, <https://www.theguardian.com/business/2015/aug/19/lithium-battery-review-boeing-dreamliner-fire-heathrow> (accessed: March 2021).
- [7] UN Bans Lithium Batteries as Cargo on Passenger Planes. BBC News, February 23, 2016, sec. Technology, **2016**, <https://www.bbc.com/news/technology-35643213> (accessed: March 2021).
- [8] Samsung to Recall Galaxy Note 7 Smartphone Over Reports of Fires – WSJ, <https://www.wsj.com/articles/samsung-to-recall-galaxy-note-7-smartphone-1472805076> (accessed: March 2021).
- [9] J. W. Choi, D. Aurbach, *Nat. Rev. Mater.* **2016**, *1*, 16013.
- [10] G. G. Yadav, D. Turney, J. Huang, X. Wei, S. Banerjee, *ACS Energy Lett.* **2019**, *4*, 2144.
- [11] H. Pan, Y. Shao, P. Yan, Y. Cheng, K. S. Han, Z. Nie, C. Wang, J. Yang, X. Li, P. Bhattacharya, K. T. Mueller, J. Liu, *Nat. Energy* **2016**, *1*, 16039.
- [12] G. Fang, J. Zhou, A. Pan, S. Liang, *ACS Energy Lett.* **2018**, *3*, 2480.
- [13] A. R. Mainar, O. Leonet, M. Bengoechea, I. Boyano, I. de Meatza, A. Kvasa, A. Guerfi, J. A. Blázquez, *Int. J. Energy Res.* **2016**, *40*, 1032.
- [14] Y. Li, H. Dai, *Chem. Soc. Rev.* **2014**, *43*, 5257.
- [15] J.-S. Lee, S. T. Kim, R. Cao, N.-S. Choi, M. Liu, K. T. Lee, J. Cho, *Adv. Energy Mater.* **2011**, *1*, 34.
- [16] J. F. Parker, C. N. Chervin, I. R. Pala, M. Machler, M. F. Burz, J. W. Long, D. R. Rolison, *Science* **2017**, *356*, 415.
- [17] L. Yin, J. Scharf, J. Ma, J.-M. Doux, C. Redquest, V. L. Le, Y. Yin, J. Ortega, X. Wei, J. Wang, Y. S. Meng, *Joule* **2021**, *5*, 228.
- [18] D. E. Turney, J. W. Gallaway, G. G. Yadav, R. Ramirez, M. Nyce, S. Banerjee, Y. K. Chen-Wiegart, J. Wang, M. J. D'Ambrose, S. Kolhekar, J. Huang, X. Wei, *Chem. Mater.* **2017**, *29*, 4819.
- [19] C. Leal, P. A. Lopes, A. Serra, J. F. J. Coelho, A. T. de Almeida, M. Tavakoli, *ACS Appl. Mater. Interfaces* **2020**, *12*, 3407.
- [20] Y. Li, J. Fu, C. Zhong, T. Wu, Z. Chen, W. Hu, K. Amine, J. Lu, *Adv. Energy Mater.* **2019**, *9*, 1802605.
- [21] W. Song, S. Yoo, G. Song, S. Lee, M. Kong, J. Rim, U. Jeong, S. Park, *Batteries Supercaps* **2019**, *2*, 181.
- [22] J. Fu, Z. P. Cano, M. G. Park, A. Yu, M. Fowler, Z. Chen, *Adv. Mater.* **2017**, *29*, 1604685.
- [23] L. Lyu, Y. Gao, Y. Wang, L. Xiao, J. Lu, L. Zhuang, *Chem. Phys. Lett.* **2019**, *723*, 102.
- [24] M. Ma, J. P. Tu, Y. F. Yuan, X. L. Wang, K. F. Li, F. Mao, Z. Y. Zeng, *J. Power Sources* **2008**, *179*, 395.
- [25] K. Bass, P. J. Mitchell, G. D. Wilcox, J. Smith, *J. Power Sources* **1991**, *35*, 333.
- [26] J. Shin, J.-M. You, J. Z. Lee, R. Kumar, L. Yin, J. Wang, Y. S. Meng, *Phys. Chem. Chem. Phys.* **2016**, *18*, 26376.
- [27] G. G. Yadav, C. Jungsang, X. Wei, M. Nyce, S. Banerjee, *Zinc Electrodes with High Capacity Utilizations*, Google Patents, XXXX **2020**.
- [28] X. Wei, M. Nyce, G. G. Yadav, A. Couzis, S. Banerjee, WO2017070340A1, **2021**.
- [29] C. Zhang, J. M. Wang, L. Zhang, J. Q. Zhang, C. N. Cao, *J. Appl. Electrochem.* **2001**, *31*, 1049.
- [30] J.-S. Chen, L.-F. Wang, *J. Appl. Electrochem.* **1996**, *26*, 227.
- [31] A. Mitha, A. Z. Yazdi, M. Ahmed, P. Chen, *ChemElectroChem* **2018**, *5*, 2409.
- [32] J. F. Parker, E. S. Nelson, M. D. Wattendorf, C. N. Chervin, J. W. Long, D. R. Rolison, *ACS Appl. Mater. Interfaces* **2014**, *6*, 19471.
- [33] J. F. Parker, C. N. Chervin, E. S. Nelson, D. R. Rolison, J. W. Long, *Energy Environ. Sci.* **2014**, *7*, 1117.
- [34] T. P. Dirkse, R. Timmer, *J. Electrochem. Soc.* **1969**, *116*, 162.
- [35] T. S. Lee, *J. Electrochem. Soc.* **1971**, *118*, 1278.
- [36] J. Liu, C. Xu, Z. Chen, S. Ni, Z. X. Shen, *Green Energy Environ.* **2018**, *3*, 20.
- [37] J. P. Allen, D. O. Scanlon, G. W. Watson, *Phys. Rev. B* **2011**, *84*, 115141.
- [38] C. P. Wales, J. Burbank, *J. Electrochem. Soc.* **1959**, *106*, 885.
- [39] J. McMillan, *Chem. Rev.* **1962**, *62*, 65.
- [40] R. F. Amlie, P. Rüetschi, *J. Electrochem. Soc.* **1961**, *108*, 813.
- [41] R. Kumar, K. M. Johnson, N. X. Williams, V. Subramanian, *Adv. Energy Mater.* **2019**, *9*, 1803645.
- [42] L. Su, L. Liu, B. Liu, J. Meng, X. Yan, *Iscience* **2020**, *23*, 100995.
- [43] X. Wei, D. Desai, G. G. Yadav, D. E. Turney, A. Couzis, S. Banerjee, *Electrochim. Acta* **2016**, *212*, 603.
- [44] P. Bonnicks, J. R. Dahn, *J. Electrochem. Soc.* **2012**, *159*, A981.
- [45] R. Franke-lang, T. Arlt, I. Manke, J. Kowal, *J. Power Sources* **2017**, *370*, 45.
- [46] T. Arlt, D. Schröder, U. Krewer, I. Manke, *Phys. Chem. Chem. Phys.* **2014**, *16*, 22273.
- [47] J. S. Ko, A. B. Geltmacher, B. J. Hopkins, D. R. Rolison, J. W. Long, J. F. Parker, *ACS Appl. Energy Mater.* **2019**, *2*, 212.
- [48] A. Yermukhambetova, C. Tan, S. R. Daemi, Z. Bakonov, J. A. Darr, D. J. L. Brett, P. R. Shearing, *Sci. Rep.* **2016**, *6*, 35291.
- [49] M. K. Christensen, J. K. Mathiesen, S. B. Simonsen, P. Norby, *J. Mater. Chem. A* **2019**, *7*, 6459.
- [50] O. O. Taiwo, D. P. Finegan, J. M. Paz-Garcia, D. S. Eastwood, A. J. Bodey, C. Rau, S. A. Hall, D. J. L. Brett, P. D. Lee, P. R. Shearing, *Phys. Chem. Chem. Phys.* **2017**, *19*, 22111.
- [51] J. F. Bonk, A. B. Garrett, *J. Electrochem. Soc.* **1959**, *106*, 612.
- [52] K. Takeda, T. Hattori, *J. Electrochem. Soc.* **1999**, *146*, 3190.
- [53] S. Berchmans, A. J. Bandodkar, W. Jia, J. Ramírez, Y. S. Meng, J. Wang, *J. Mater. Chem. A* **2014**, *2*, 15788.
- [54] 24K Pure Gold Plating Solution – Bath, <https://www.goldplating.com/products/24k-pure-gold-solution> (accessed: March 2021).
- [55] P. Arora, Z. (John) Zhang, *Chem. Rev.* **2004**, *104*, 4419.
- [56] M. T. Tsehaye, F. Alloin, C. Iojoiu, R. A. Tufa, D. Aili, P. Fischer, S. Velizarov, *J. Power Sources* **2020**, *475*, 228689.
- [57] Innovia Films – BOPP Film for Food and Tobacco Packaging and Labels, <http://www.innoviafilms.com/> (accessed: March 2021).
- [58] P. Viola, W. M. Wells III, *International journal of computer vision* **1997**, *24*, 137.
- [59] A. Collignon, F. Maes, D. Delaere, D. Vandermeulen, P. Suetens, G. Marchal, *Information Processing in Medical Imaging* **1995**, *3*, 263.
- [60] J. Pluim, J. Maintz, M. Viergever, *IEEE Transactions on Medical Imaging* **2003**, *22*, 986.
- [61] A. Roche, G. Malandain, X. Pennec, N. Ayache, in *Medical Image Computing and Computer-Assisted Intervention—MICCAI'98*, (Eds.: W. M. Wells, A. Colchester, S. Delp), Springer, Berlin **1998**, pp. 1115–1124.
- [62] C. Zelger, J. Laumen, A. Laskos, B. Gollas, *Electrochim. Acta* **2016**, *213*, 208.
- [63] M. J. D'Ambrose, D. E. Turney, G. G. Yadav, M. Nyce, S. Banerjee, *ACS Appl. Energy Mater.* **2021**, *4*, 3381.